PNAS
www.pnas.org

Supplementary Information for
Ultrafast Photooxidation of Protein-Bound Anionic Flavin Radicals

Bo Zhuang, Rivo Ramodiharilafy, Ursula Liebl, Alexey Aleksandrov*, and Marten H. Vos*

LOB, CNRS, INSERM, École Polytechnique, Institut Polytechnique de Paris, 91128 Palaiseau, France

*Alexey Aleksandrov

Email: alexey.aleksandrov@polytechnique.edu

*Marten H. Vos

Email: marten.vos@polytechnique.edu

This PDF file includes:

Supplementary Information Text

SI Methods

Sample Preparations.

GOX from *Aspergillus niger*, COX from *Arthrobacter sp.*, MSOX from *Bacillus sp.* and DAAO from porcine kidney were purchased from Sigma-Aldrich. GOX, COX and MSOX were used without further purification. DAAO from Sigma-Aldrich contained substantial excess free flavin, which was removed before use by washing with excess buffer followed by concentrating with a 30-kDa cutoff Amicon Ultra 4 filter (Millipore) three times (cf. Ref. (1)). The gene *pa4202* from *Pseudomonas aeruginosa* PAO1, coding for NMO, was inserted into plasmid pQE60 (Qiagen) via unique *NcoI* and *BamHI* restriction sites. The construct, carrying a hexahistidine (6xHis)-tag at its carboxyl terminus, was confirmed by DNA sequencing. Expression of the recombinant NMO protein in *E. coli* BL21DE3 was induced by adding 1 mM IPTG to early exponential phase cultures. 6xHis-tagged proteins were purified from cell-free extracts by gravity-flow chromatography on Ni-TED columns (Macherey Nagel), followed by subsequent imidazole removal as described previously (2).

Unless stated otherwise, phosphate buffer (~50 mM) was used for the pH range from 5.5 to 8.5, glycine-NaOH buffer (~80 mM) was used for the pH range from 9.0 to 13.0, and protein samples were prepared with a flavin concentration of 100–200 µM in 1-mm path length quartz cells. Flavins in the oxidized form were studied under aerobic conditions. Anionic flavin radicals were obtained in extensively degassed samples, either by chemical reduction or photoreduction. At pH 7.6, pH 10.1 or pH 13.0, to generate $FAD^{\bullet-}$ in GOX, FAD_{ox} was reduced by a 2-fold molar excess of sodium dithionite ($Na_2S_2O_4$) under anaerobic conditions. The photoreduction of GOX into the $FAD^{\bullet-}$ form was carried out as follows: the protein sample solution at pH 10.1 and in the presence of 10 mM EDTA or 1 mM 2-mercaptoethanol (2-ME) was irradiated by a 450 nm LED (0.45 W) for 90 minutes in an ice-bath (1, 3). $FADH^-$ in GOX was prepared by reduction under anaerobic conditions with a large excess of D(+)-glucose at pH 7.6. To obtain $FAD^{\bullet-}$ in COX, a 1.2-fold molar excess of $Na_2S_2O_4$ was added to the oxidized protein sample at pH 8.1 under anaerobic conditions, and the mixture was incubated at room temperature for 2 hours. $FAD^{\bullet-}$ in MSOX was prepared by reduction with a 2-fold molar excess of $Na_2S_2O_4$ at pH 8.5. $FAD^{\bullet-}$ in DAAO was produced by photoreduction in the presence of 1 mM 2-ME via a process similar to that described above for GOX, with an illumination time of 5 minutes. To obtain $FMN^{\bullet-}$ in NMO, reduction of NMO with propionate 3-nitronate was conducted in Tris-buffered saline (TBS) buffer at pH 8.0 as described in Ref. (4). The reduction processes were followed by monitoring steady-state absorption spectra with a Shimadzu UV–Vis 1700 spectrophotometer or fluorescence spectra with a Cary Eclipse fluorometer. The experimental conditions for preparing reduced flavins are also summarized in Table S1.

Spectroscopic Measurements.

The setup for time-resolved fluorescence employs a Kerr gate (5). Briefly, part of the 780 nm output from the Ti:sapphire laser/amplifier system (Quantronix Integra-C) operating at 0.5 kHz was passed through a BBO crystal, yielding an excitation pulse centered at 390 nm. The remaining 780 nm beam was directed through a motorized delay-line and focused into the Kerr medium where it spatially overlapped the fluorescence from the sample. The gated fluorescence was then detected with spectral resolution using a polychromator and a CCD camera configured as an array detector. Kerr media with different time-resolution/sensitivity compromises were used, i.e., suprasil (response time ~200 fs), benzene (response time ~400 fs) and CS_2 (response time ~1 ps).

Multicolor time-resolved absorption spectra were recorded by the pump–probe technique on an instrument operating at 500 Hz, as described previously (2, 6). Pump pulse centered at 390 nm were obtained by frequency-doubling the fundamental beam. Pump pulses centered at 520 nm were obtained with a non-collinear optical parametric amplifier and tailored with a sharp-edge interference filter. Continuum broadband pulses that were passed through a prism-compressor were used as the probe. The instrument response function has a 20-80% rise time of 100 fs as determined from experiments on carboxy-myoglobin. Given the amplitudes of the cross-phase modulation artifacts, which were minimal at the minimum of the probe compression curve (cf. Fig. S14) with respect to the flavoprotein signals, we estimate the effective determination of the intrinsic rise time of the signals at ~100 fs. Pump and probe beams were set at the magic angle (54.7°) to

record the isotropic spectra. Additionally, parallel and perpendicular pump–probe configurations were used for recording the transient anisotropy data, where the polarization of the probe beam remains unchanged, and the pump beam polarization is rotated using a λ/2 plate. The excitation power was adapted such that each shot of the pump beam excited less than 10% of the sample. The concentrations of excited molecules were determined using $[Ru(bpy)_3]Cl_2$ as a reference (6), as detailed in *Note 4*. Unless indicated otherwise, for reduced protein samples, those reduced chemically were used in time-resolved spectroscopic measurements, and all the measurements were carried out at 10 °C. Global analysis of the data was performed using the Glotaran program based on the R-package TIMP (7).

Computer Simulations.

Geometry optimizations in vacuum were performed at the ωB97X-D3/ma-def2-TZVP level (8, 9). Vibrational analysis was performed on the optimized structures to confirm that the optimization converged to a minimum. To calculate the free energy changes of redox reactions, single point energies were calculated on the optimized geometries at the PWPB95-D4/def2-QZVPP level, as suggested in Ref. (10), while the thermostatistical corrections at 298.15 K were obtained from the frequency analysis at the ωB97X-D3/ma-def2-TZVP level. The SMD solvation model (11) was used to estimate the solvation energies in the aqueous solution at the M06-2X/6-31G* level (12). These DFT calculations were carried out using the ORCA program (version: 4.2) (13).

MD simulations of GOX were carried out using the NAMD program (version 2.13) (14). The structure of GOX from *Aspergillus niger* was taken from the Protein Data Bank (PDB entry: 1CF3). The CHARMM36m force field was used for the protein residues (15) and the TIP3P model for water (16); a recently developed force field for flavins was used to describe $FAD^{\bullet-}$ and $FADH^-$ (17). The protonation states of all titratable residues other than His516 were assigned based on a PROPKA 3.1 analysis (18), and verified by ideal stereochemistry. The pK_a value of His516 in the active site of GOX and in the presence of $FAD^{\bullet-}$ or $FADH^-$ was specifically calculated using computationally intensive MDFE simulations (19), as described in *Note 6*. A disulfide bridge was created between Cys164 and Cys206. The protein was placed in a cubic water box, at least 12 Å away from each of the box faces. Periodic boundary conditions were assumed, and an appropriate number of potassium counterions was included to neutralize the net charge of the system. Long-range electrostatic interactions were computed using the particle mesh Ewald method (20). The integration time step was set at 2 fs. After energy minimization, the system was equilibrated first in an NVT ensemble for 50 ps, followed by a 500 ps simulation in the NPT ensemble, at 295 K and 1.0 atm pressure before the production runs. The Berendsen thermostat and barostat were employed, with a relaxation time of 500 fs and 4 timesteps between position rescalings (21).

For GOX, the spectral properties of $FAD^{\bullet-}$ in the resting state, as well as transient FAD_{ox} and reduced His559 (in the neutral radical form, $HisH_2^{\bullet}$), were calculated via a QM/MM approach, using the pDynamo program (version 1.9.0) (22) coupled with the ORCA package. 20 structures taken each 7.5 ns from the 150 ns MD trajectories (Fig. S24) were used for the QM/MM calculations. Electrostatic interactions between the QM and MM regions were treated using the electrostatic embedding. The QM region included the isoalloxazine ring moiety of FAD or the side chain of His559, with the remaining groups of FAD, protein residues and water molecules (580 protein residues and 20061 water molecules) included to the MM region and described with the same force fields as in the MD simulations (Fig. S25). To model the product state following the photooxidation reaction, at the MM level, the force field parameters of FAD were modified to correspond to FAD_{ox} (17) and those of His559 to $HisH_2^{\bullet}$. In particular, the CHELPG atomic charges (23) for $HisH_2^{\bullet}$ were obtained by fitting the QM electrostatic potential around the solutes after geometry optimizations in vacuum at the QM level (ωB97X-D3/ma-def2-TZVP, Table S6). For the bonded terms in the force field model, we used those from the standard force fields of doubly protonated histidine, as justified in Refs. (6, 24) The QM region was first optimized by energy minimization with the MM regions fixed using the L-BFGS optimization method at the (U)B3LYP/6-31+G* level (25, 26), with a RMS gradient tolerance of 0.2 kcal/(mol Å) as the convergence criterion. Excitation energies and oscillator strengths of 30 excited states were then estimated using TDDFT calculations performed

at the same QM level. The results of all snapshots were broadened with a Gaussian line shape (FWHM: 0.42 eV) and then averaged.

HOMO and LUMO energy levels of $FAD^{\bullet-}$ were calculated in a vacuum and in GOX. Those in a vacuum are based on the geometry optimized at the ωB97X-D3/ma-def2-TZVP level, while in GOX the calculations were performed at the ωB97X-D3/ma-def2-TZVP level considering the effects of the protein environment, based on QM/MM-optimized geometries at the UB3LYP/6-31+G* level, and averaged for 20 snapshots along the MD trajectories to give the results shown in Fig. 1D of the main text.

The PB equation was solved using the CHARMM program (version: 45b2) (27) to evaluate electrostatic energies in the protein-water systems. The dielectric constant was set to 2 inside the protein and 80 for water. The protein dielectric constant was higher than 1 to include implicitly the electronic relaxation, which is absent in the additive C36 force field (28). The PB energies were computed using the focusing method with a coarse grid of 0.8 Å resolution and a fine grid with 0.4 Å resolution, based on the coordinates of 100 snapshots taken each 1.5 ns from the MD trajectories. The partial charges in the MM region of the model were set accordingly to represent the system before and after the ET reaction. Combined with the calculations of redox free energy changes in solution based on the DFT calculations described above, the change of free energy due to the ET reaction in the protein environment can be estimated (*Note 7*).

Note 1. Steady-state reduction of oxidized flavins

The experimental conditions for preparing reduced flavin species in this study are summarized in Table S1. The results are similar to those reported in the literature (as an illustration, the process of reduction of FAD_{ox} in COX by $Na_2S_2O_4$ is given in the inset of Fig. S2), except for $FAD^{\bullet-}$ in DAAO. During the photoreduction of DAAO, when the reaction reached the maximum radical formation (judged by whether pursuing the illumination would reduce the overall absorbance in the visible range, which is an indication of accumulation of fully reduced flavins), we obtained a spectrum that appears to have a FAD_{ox} contribution (Fig. S3). This is most likely due to residual free flavin present in our sample (a commercial product purchased from Sigma and subsequently purified by repeated washing steps with excess buffer), which after illumination is present in an equilibrium between the oxidized and fully reduced forms because the redox potentials for the oxidized/semi-reduced and semi-reduced/fully-reduced couples of free flavins in solution are close. We also attempted photoreduction of DAAO purchased from Abnova, which did not contain excess free flavin. However, it appeared unstable in solution.

Previous reports by Massey *et al.* have proposed that the photoreduction of oxidized flavins in flavoproteins occurs mostly with a trace amount of free flavin in the protein sample acting as catalyst, and the reaction proceeds via an exchange of electrons between fully reduced free flavin in solution and protein-bound oxidized flavin, involving equilibria between oxidized, semi-reduced and fully reduced forms (29, 30). Given this mechanism, it might be difficult to achieve a 100%-yield formation of the anionic radical form, as trace amounts of oxidized flavin, fully reduced flavin, or even unknown residue–flavin adducts (see below) can remain present in the sample. This can complicate the time-resolved measurements under 390-nm excitation, because those flavin species usually absorb in the near ultraviolet range (Fig. 1C of the main text, Fig. S9). For GOX, the amount of dissociated free flavin is rather low, as without adding external free flavin the photoreduction is extremely slow (compared with, e.g., DAAO, where the photoreduction can proceed very rapidly).

Note 2. Fluorescence of flavin species in GOX and COX

Fluorescence of flavin species in COX exhibits complex behaviors. For the as-prepared COX sample under oxidizing conditions, time-resolved fluorescence measurements show that its fluorescence decays in a biphasic manner with an ultrafast 300-fs phase and a relatively long-lived 440-ps phase (Fig. S7a, Table S2). In the active site of COX, there are electron-donating residues, Tyr465 and Trp61, located close to the flavin (Fig. S10). Therefore, the 300-fs phase can be assigned to the fluorescence of FAD_{ox} quenched by ultrafast photoinduced ET from those nearby

residues, which is a phenomenon commonly observed in flavoproteins (24, 31, 32). On the other hand, steady-state fluorescence excitation and emission spectra (Fig. S9), which essentially reflect the integrated fluorescence of the long-lived phase in the time-resolved measurements, clearly demonstrate that the 440-ps phase results from a species different from FAD_{ox}, with an absorption maximum at ~400 nm. The spectral features of this unknown species highly resemble those of a residue–flavin adduct in COX obtained at a high pH, which has been proposed to be a C4a-N-histidyl-FAD adduct (33).

For the reduced COX sample, as discussed in the main text and illustrated in Fig. S7, in the time-resolved measurements, the reduction reaction appears to diminish the overall intensities of the fluorescence rather than result in different spectra and dynamics. The steady-state fluorescence spectra (Fig. S8) further confirm that the integrated fluorescence observed under 400-nm excitation cannot be due to $FAD^{\bullet-}$, as we did not observe any emission when exciting the sample at 500 nm where $FAD^{\bullet-}$ absorbs.

Altogether, we ascribe the fluorescence detected in the reduced COX sample to a trace amount of FAD_{ox} (290-fs phase) and the residue–flavin adduct or other unidentified reaction by-products (320-ps phase) present in the sample. Any emission from $FAD^{\bullet-}$ must decay on a much shorter timescale, exceeding the temporal resolution of our measurements.

Note 3. Transient absorption measurements under different conditions

The transient absorption spectra of $FADH^-$ in GOX (Figs. S11 and S12) are consistent with those reported in the literature (34). As discussed in the main text, the spectral features and dynamics of excited-state $FADH^-$ resemble the long-lived phase of $FAD^{\bullet-}$ in GOX (Fig. S15), indicating that the complexity of the transient absorption spectra of $FAD^{\bullet-}$, with two additional small phases under 390-nm excitation, can be attributed to the presence of a trace amount of other flavin species in a different redox state. This may also be the case for COX and MSOX (Figs. S16 and S17), as we have demonstrated above a slightly inhomogeneous composition of the reduced sample for these species. For MSOX, the spectral features of the 1.7 ps phase (Fig. S17) are indeed very similar to what we have observed upon excitation of FAD_{ox} at 390 nm (Fig. S18).

As shown in Fig. S19, $FAD^{\bullet-}$ in GOX prepared via different methods or at different pH exhibits similar transient absorption spectra. Yet, the overall shapes of the ~20-ps phases of the different samples slightly vary, whereas the ground-state absorption spectrum of FAD_{ox} in GOX does not perceptibly depend on the pH (Fig. S20). This suggests that the spectral properties of the transiently formed FAD_{ox} (or the electron acceptor species) are sensitive to the local protein environment on an ultrafast timescale. The variation in relative amplitudes of the ~2 ps and ~ns phases might reflect variation in the yields of $FAD^{\bullet-}$ under different conditions.

Note 4. Determination of the initial concentrations for transient species

Using $[Ru(bpy)_3]Cl_2$ as a reference, we determined the initial concentrations of excited $FAD^{\bullet-}$ in GOX in transient absorption measurements. Under the same excitation conditions, we have (24, 35):

$$c^*_{FAD^{\bullet-}} = \frac{c^*_{Ru}\left(1-10^{-A^{gs}_{FAD^{\bullet-}}}\right)}{1-10^{-A^{gs}_{Ru}}} \qquad (\mathrm{eq.\,s1})$$

where $c^*_{FAD^{\bullet-}}$ is the concentration of excited $FAD^{\bullet-}$, c^*_{Ru} is the concentration of the excited Ru complex, $A^{gs}_{FAD^{\bullet-}}$ and A^{gs}_{Ru} are the ground-state absorbance of $FAD^{\bullet-}$ in GOX, and the $[Ru(bpy)_3]^{2+}$ sample at the excitation wavelength, respectively.

Upon excitation, $[Ru(bpy)_3]^{2+}$ undergoes a charge transfer reaction resulting in a long-lived metal-to-ligand charge transfer (MLCT) state. The reaction has a 100% quantum yield and the difference of molar extinction coefficient of $[Ru(bpy)_3]^{2+}$ at 450 nm following this reaction ($\Delta\varepsilon_{450}$) has been reported to be $-1.1 \times 10^4\ M^{-1}cm^{-1}$ (36). Therefore, c^*_{Ru} can be calculated from a reference transient absorption measurement, and used to estimate $c^*_{FAD^{\bullet-}}$ according to eq. s1. Using this approach, in our measurement of GOX, $c^*_{FAD^{\bullet-}}$ is estimated to be 2.2×10^{-2} mM. Alternatively, by assuming a

photooxidation reaction with 100% yield, $c^*_{FAD^{\bullet-}}$ can also be estimated from the initial amplitude (at 450 nm) of the product state, by dividing it with the difference of ground-state extinction coefficients $(\varepsilon_{FAD_{ox}} - \varepsilon_{FAD^{\bullet-}})_{450}$, which gives a value of 2.7×10^{-2} mM. The fact that the difference between the two estimations is small further supports the assumption of a photooxidation reaction with near-unity yield. It is also worth noting that the latter calculation may overestimate the concentration if a third species contributes to the transient absorption spectra in the probed region, which is very likely to be the case here.

Note 5. Calculations of anisotropy and orientation of transition dipole moments

In transient anisotropy experiments, the transient absorption spectra are measured with the pump and probe pulses polarized parallel ($\Delta A_{\parallel}$) and perpendicular ($\Delta A_{\perp}$) (37). For pumping and probing single transitions, the anisotropy r:

$$r = \frac{\Delta A_{\parallel} - \Delta A_{\perp}}{\Delta A_{\parallel} + 2\Delta A_{\perp}} \qquad (\mathrm{eq.\,s2})$$

It is related to the angle ϕ between the pumped and probed transition as:

$$r = \frac{3cos^2\phi - 1}{5} \qquad (\mathrm{eq.\,s3})$$

For pumping and probing identical or parallel transitions (ϕ = 0), r can be calculated to be 0.4 according to eq. s3.

To obtain a theoretical prediction for the transition dipole moments of an anionic flavin radical, the structure of its chromophore (lumiflavin) in the anionic radical form was optimized at the ωB97X-D3/ma-def2-TZVP level in a vacuum, and then TDDFT calculations were performed based on the optimized structure at the PEB0/ma-def2-TZVP level for 30 excited states. The result (Fig. S22) demonstrates that the two major transient bands of the anionic flavin radical in the visible/near ultraviolet range ($D_0 \rightarrow D_4$ and $D_0 \rightarrow D_6$) form a small angle (8°), which is qualitatively consistent with our experimental observations.

Note 6. MDFE simulations for pK_a calculations

The pK_a of a titratable group in the protein environment can be calculated by:

$$\mathrm{p}K_{\mathrm{a,prot}} = \mathrm{p}K_{\mathrm{a,ref}} + \frac{\Delta\Delta G}{2.303RT} \qquad (\mathrm{eq.\,s4})$$

where p$K_{a,prot}$ and p$K_{a,ref}$ are the pK_a of the titrating group in the protein and the reference model compound in the solution, respectively, and $\Delta\Delta G = \Delta G_{\mathrm{prot}} - \Delta G_{\mathrm{solv}}$ is the double free energy difference (19, 38).

To calculate $\Delta\Delta G$ we use alchemical free energy simulations (39), where the system of interest is gradually transformed from the initial state A to the final state B by modifying the energy function U, and the simplest scheme is to make U a linear function of the coupling parameter, λ:

$$U(\lambda) = (1-\lambda)U_{\mathrm{A}} + \lambda U_{\mathrm{B}} \qquad (\mathrm{eq.\,s5})$$

where U_A and U_B are the energy functions of the initial and final states. A value between 0 and 1 corresponds to a hybrid system which is a mixture of A and B. The corresponding free energy was then obtained by thermodynamic integration (TI):

$$\Delta G = \int_0^1 \langle \frac{\partial U(\lambda)}{\partial \lambda} \rangle_{\lambda} \, d\lambda \qquad (\mathrm{eq.\,s6})$$

Based on the MDFE method described above, we calculated the pK_a value of His516 in GOX in the presence of $FAD^{\bullet-}$ or $FADH^-$. The MD simulations were performed with the NAMD program (14). In particular, protein residues within a 24 Å sphere centered at the isoalloxazine ring of FAD were placed in cubic water boxes, at least 12 Å away from each of the box edges, similar to our previous studies (40, 41). Non-hydrogen atoms between 20 and 24 Å from the sphere center were harmonically restrained to their experimentally determined positions based on the crystal structure. The other settings of the system and the procedure of the equilibration run are similar to those described in for the full-protein MD simulation above. To perform free energy simulations, the λ values employed were 0.00, 0.25, 0.50, 0.75, and 1.00, and the charges in the force field were

modified accordingly to represent the deprotonation process of histidine (where the N_ε was deprotonated). 20 individual runs were performed where ΔG was calculated every 50 ns, and the production MD sampling time accumulated to 1 ms in total. The derivatives in eq. s6 were computed numerically and averaged over 500 structures from a window simulation. MDFE simulations were performed for a dipeptide with a histidine side chain immersed in a 30-Å box of water to estimate the free energy change of histidine deprotonation in solution (ΔG_{solv}). The pK_a of His516 was then computed (experimental pK_a in solvent for His_ε: 7.0) according to eq. s4. The results of the MDFE simulations are summarized in Table S5. Calculations were performed in the presence of $FADH^-$ to verify the method, since the experimental pK_a value of His516 was measured previously with this state of flavin, with a value of 8.1 determined by the reaction rates of the reduced enzyme toward O_2 (42). The result shows that, in the presence of $FADH^-$, the pK_a of His516 is calculated to be 9.6 (SD: 0.4), which is reasonably close to the experimental value. Thus, in the experimental pH range where our measurements were conducted, His516 prefers a doubly protonated form, $HisH_2^+$.

Note 7. Calculation of free energy changes of redox processes

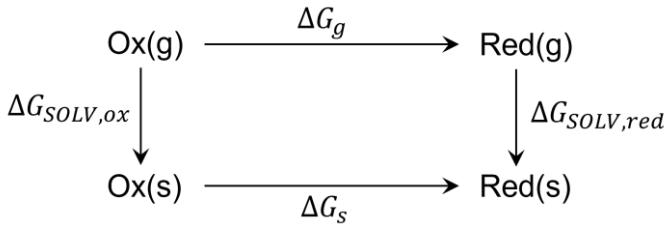

As shown in the scheme above, the change of free energy of the redox reaction in solvent, ΔG_s, can be calculated from its components by introducing a thermodynamic cycle:

$$\Delta G_s = \Delta G_g + \Delta G_{SOLV,red} - \Delta G_{SOLV,ox} \qquad (\text{eq. s7})$$

$$\Delta G_g = G_{g,red} - G_{g,ox} - 2.5RT \qquad (\text{eq. s8})$$

where $G_{g,red}$ and $G_{g,ox}$ are the energies of the redox pair in the gas phase, $\Delta G_{solv,ox}$ and $\Delta G_{solv,red}$ are solvation energies of the oxidized and reduced species in water, respectively, and the $2.5RT$ term corresponds to the thermal energy of the free electron (43).

Using the energies estimated by DFT calculations (Table S7), the change of free energy of the ET reaction, $FAD^{\bullet-}/HisH_2^+ \rightarrow FAD_{ox}/HisH_2^\bullet$, in aqueous solution, $\Delta G_{ET,solv}$, can be computed as:

$$\Delta G_{ET,solv} = \Delta G_{s,HisH_2^+/HisH_2^\bullet} - \Delta G_{s,FAD_{ox}/FAD^{\bullet-}} \qquad (\text{eq. s9})$$

to be 189.1 kJ/mol or 1.96 eV.

In order to compute the change of free energy due to the ET reaction in the protein environment, the PB equation was solved using the following parameters. The dielectric constant was set to 2 inside the protein and 80 for water. The protein dielectric constant was higher than 1 to include implicitly the electronic relaxation, which is absent in the additive C36 force field (28) and chosen to be 2 to correspond to an unrelaxed protein environment. The PB energies were computed using the focusing method with a coarse grid of 0.8 Å resolution and a fine grid with 0.4 Å resolution. The partial charges in the MM region of the model were set accordingly to represent the system before and after the ET reaction. The difference of electrostatic energies of the systems before and after the ET reaction, $\Delta\Delta G_{ES}$, was then computed as:

$$\Delta\Delta G_{ES} = \Delta G_{ES,post} - \Delta G_{ES,pre} \qquad (\text{eq. s10})$$

where $\Delta G_{ES,pre}$ and $\Delta G_{ES,\,post}$ are obtained from the solution of the PB equation (44). By performing the calculations on the structures of 100 snapshots taken each 1.5 ns from the MD trajectories of the GOX simulation, the average of $\Delta\Delta G_{ES}$ is calculated to be 5.3 (SD:1.1) kcal/mol or 0.23 (SD: 0.05) eV.

For comparison, we also tested the ET energy with the higher protein dielectric constant of 4, which decreases the free energy difference in protein by a modest 2.6 kcal/mol (corresponding to only 0.1 eV) relative to the result obtained with the dielectric constant of 2.

Supplementary Figures

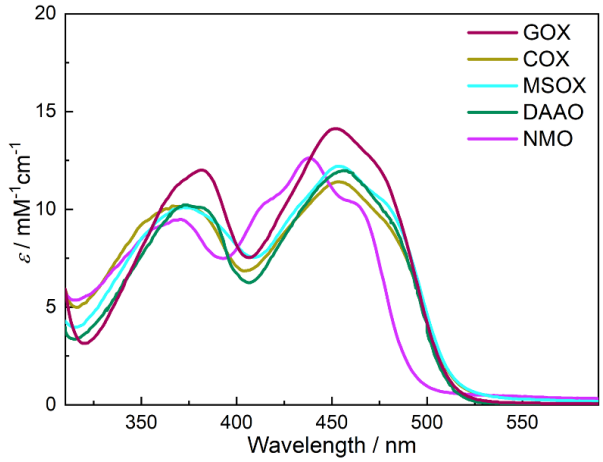

Fig. S1. Steady-state absorption spectra of oxidized flavins in GOX, COX, MSOX, DAAO and NMO under aerobic, non-reducing conditions.

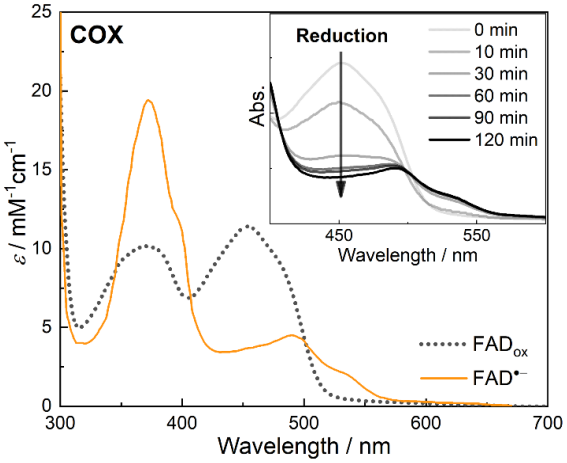

Fig. S2. Chemical reduction of FAD_{ox} and formation of $FAD^{\bullet-}$ in COX under anaerobic conditions. The inset shows the spectral changes recorded at different time points during the reduction process with $Na_2S_2O_4$.

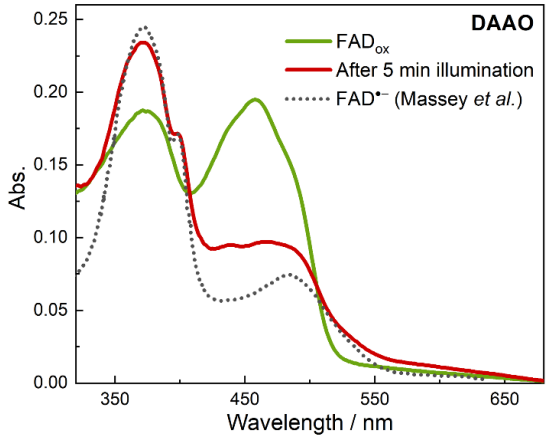

Fig. S3. Photoreduction of FAD_{ox} in DAAO in the presence of 2-ME. The illumination was stopped before the fully reduced flavin started to accumulate in the sample. The spectrum of $FAD^{\bullet-}$ in DAAO reported by Massey *et al.* (3) is shown as a dotted line for comparison.

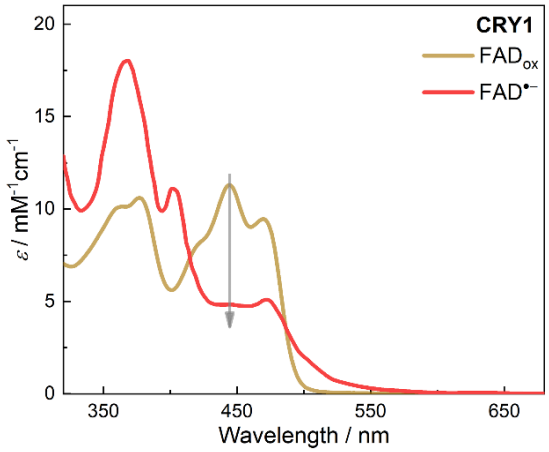

Fig. S4. Steady-state absorption spectra of FAD_{ox} and $FAD^{\bullet-}$ in insect cryptochrome (45).

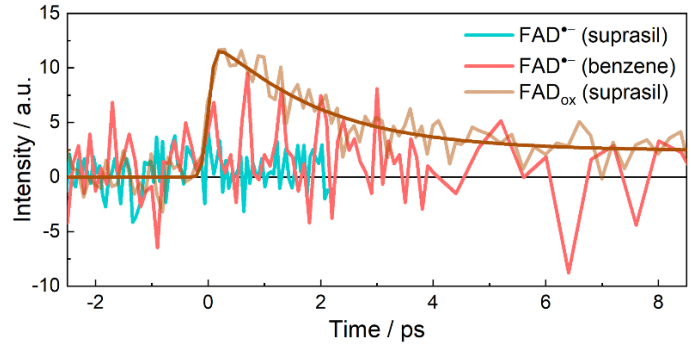

Fig. S5. Time-resolved fluorescence measurements of $FAD^{\bullet-}$ and FAD_{ox} in GOX with benzene or suprasil as Kerr medium. The smooth brown curve represents a biexponential fit of the FAD_{ox} data with time constants of 1.1 ps and 4.3 ps (cf. Ref. (32)).

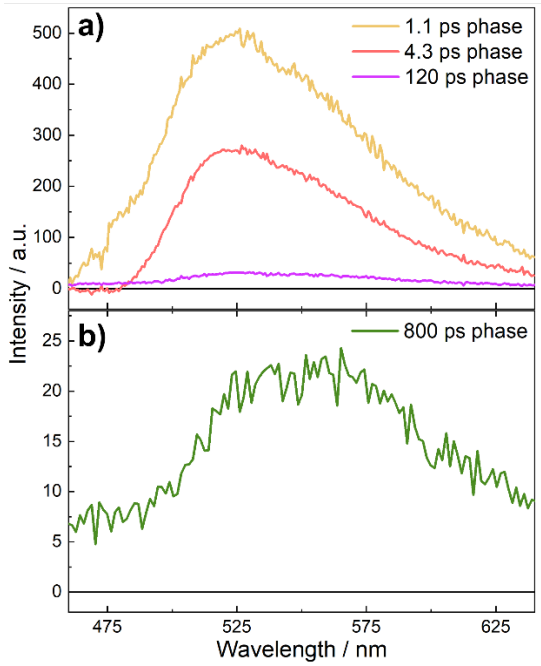

Fig. S6. DAS from the global analysis of fluorescence decays of FAD_{ox} (a) and $FADH^{-}$ (b) in GOX with CS_2 as Kerr medium.

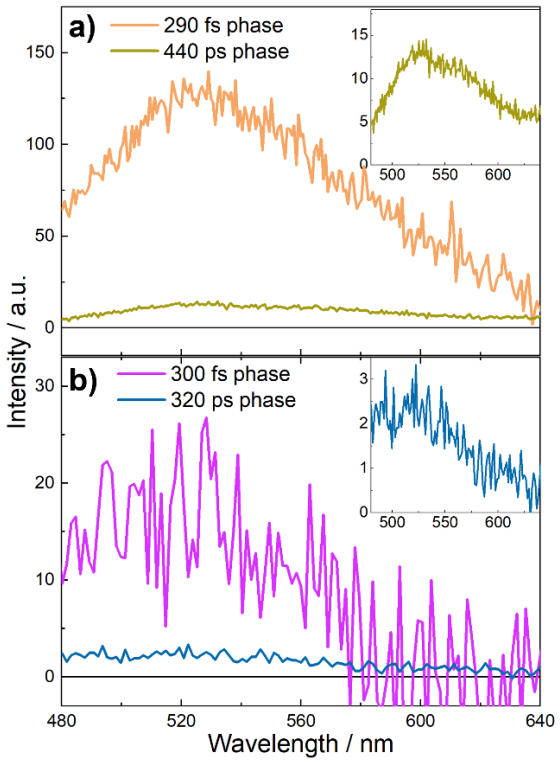

Fig. S7. DAS from the global analysis of fluorescence decays of COX under oxidizing (a) and reducing (b) conditions with benzene as Kerr medium.

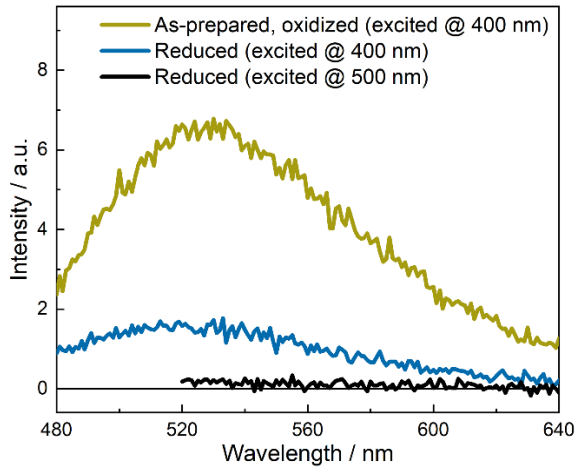

Fig. S8. Steady-state fluorescence of COX under oxidizing (a) and reducing (b) conditions.

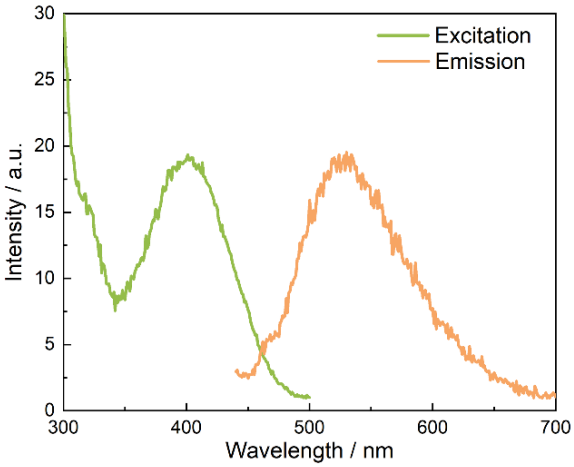

Fig. S9. Steady-state fluorescence excitation (monitored at 550 nm) and emission (excited at 400 nm) spectra of the as-prepared, oxidized sample of COX.

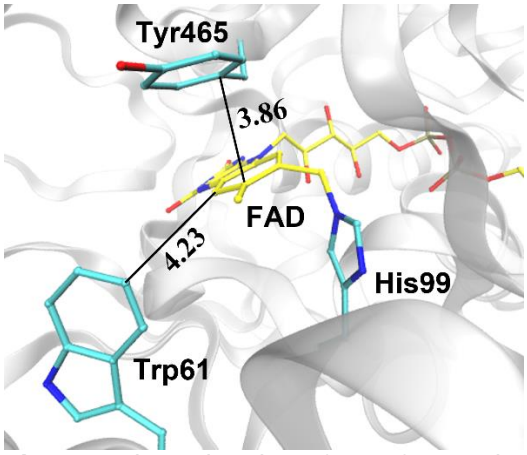

Fig. S10. The active sites of COX from *Arthrobacter globiformis* (S101A variant; PDB entry: 3NNE). The shortest ring-to-ring distances between the flavin and close-by electron-donating residues are shown in Å.

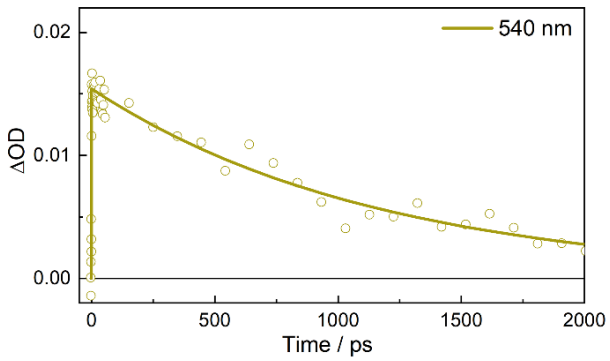

Fig. S11. Isotropic transient absorption kinetics of $FADH^-$ in GOX at 540 nm upon excitation at 390 nm.

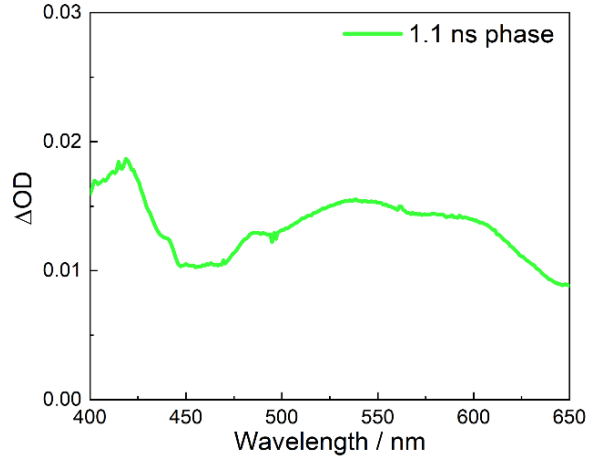

Fig. S12. DAS of isotropic transient absorption data of $FADH^-$ in GOX under excitation at 390 nm.

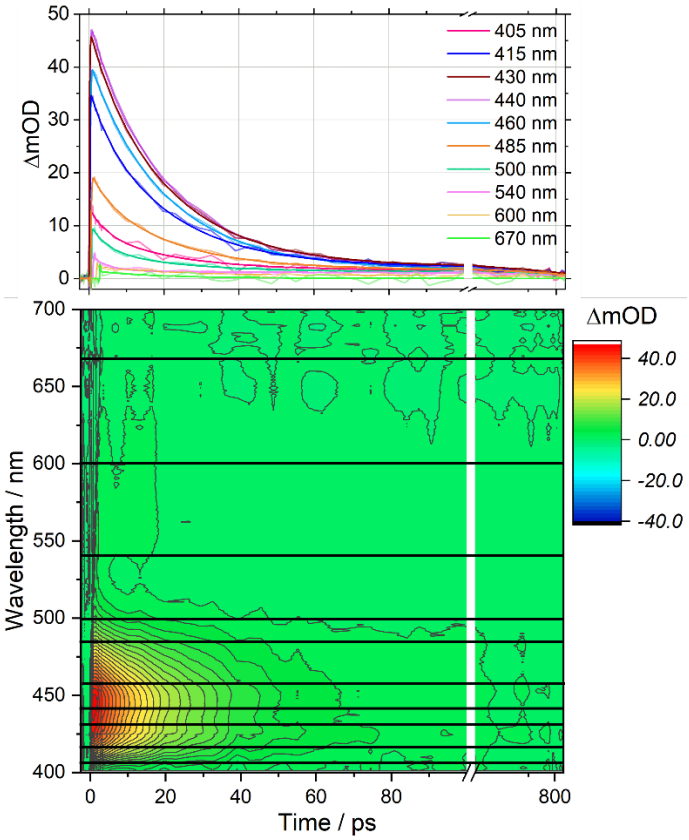

Fig. S13. Two-dimensional transient absorption map (bottom panel) of $FAD^{\bullet-}$ in GOX under excitation at 390 nm and the corresponding time slices (top panel) at marked wavelengths. The time axis in both plots is linear up to 100 ps and logarithmic thereafter.

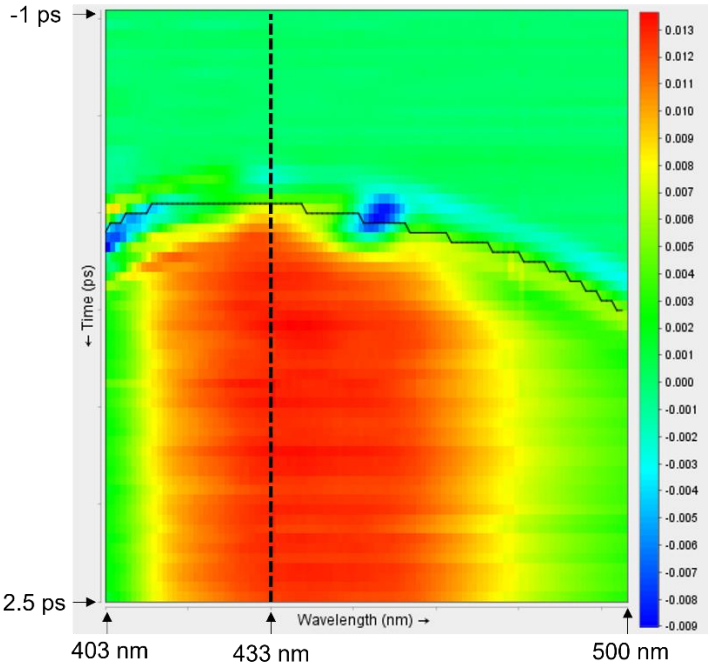

Fig. S14. Two-dimensional false color transient absorption map of $FAD^{\bullet-}$ in GOX under excitation at 390 nm in the range of -1 ps to 2.5 ps. The fitted temporal dispersion is shown in solid line. The dashed line corresponds to the trace in Fig. 3A, *inset.*

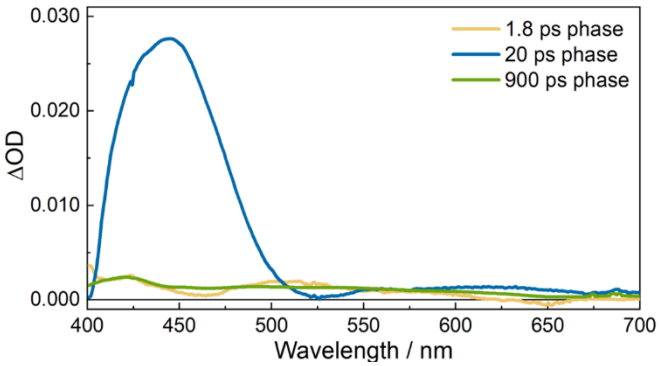

Fig. S15. DAS of isotropic transient absorption data of $FAD^{\bullet-}$ in GOX under excitation at 390 nm.

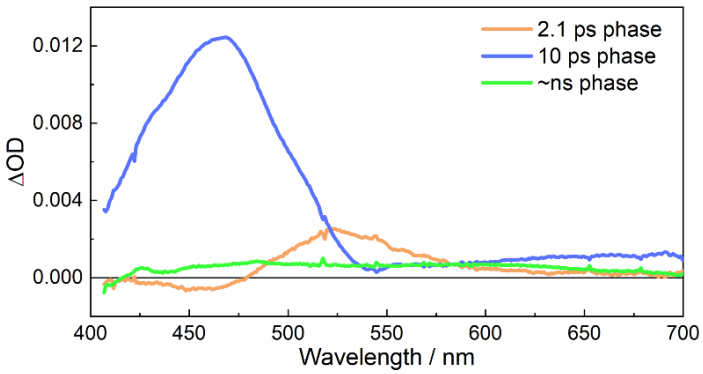

Fig. S16. DAS of isotropic transient absorption data of reduced COX under excitation at 390 nm.

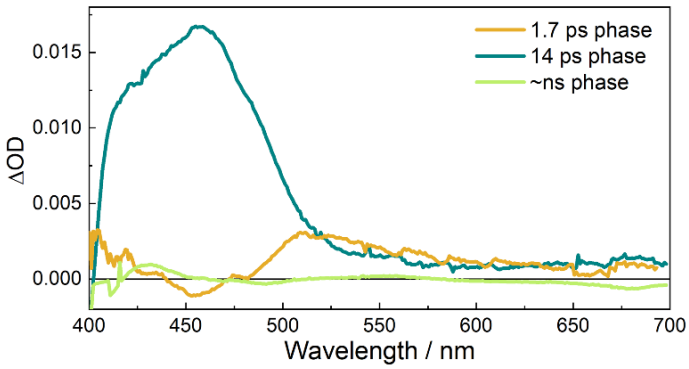

Fig. S17. DAS of isotropic transient absorption data of reduced MSOX under excitation at 390 nm.

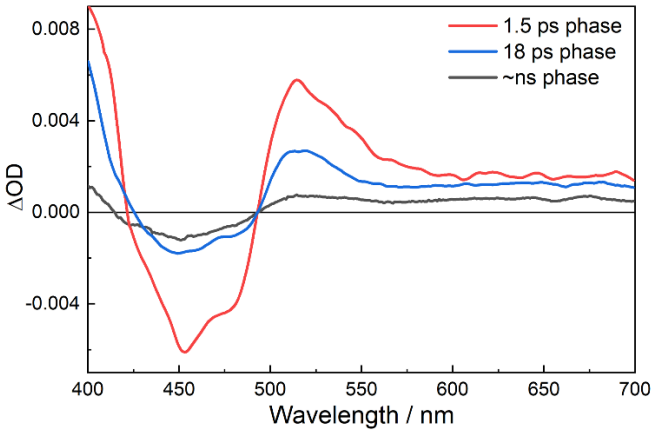

Fig. S18. DAS of isotropic transient absorption data of oxidized MSOX under excitation at 390 nm.

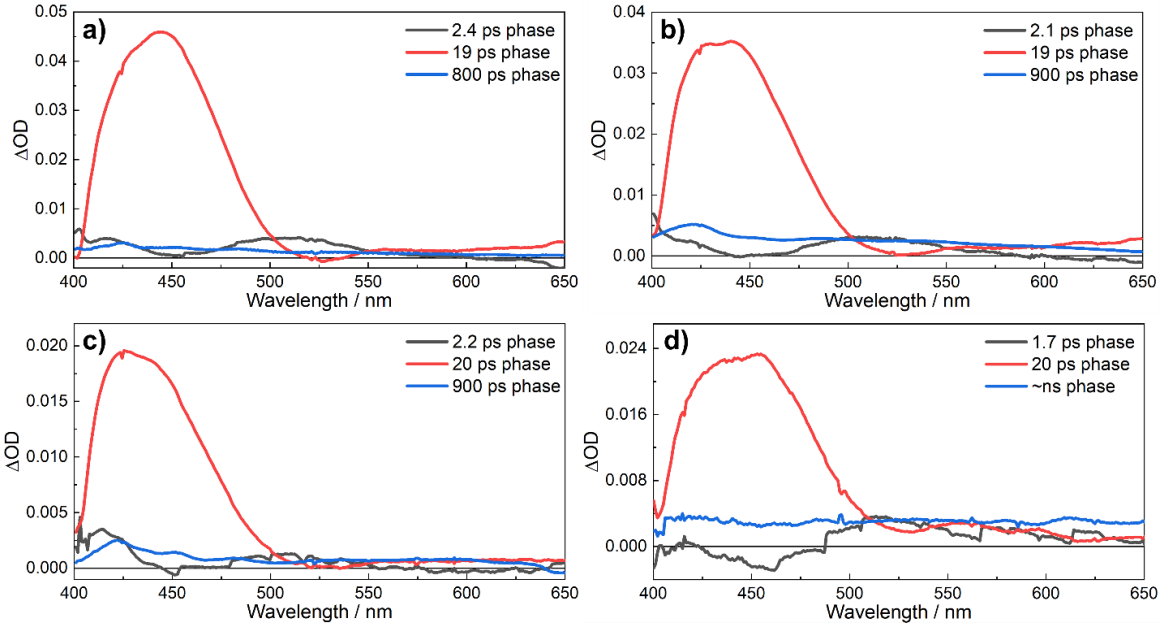

Fig. S19. DAS of isotropic transient absorption data of $FAD^{\bullet-}$ in GOX under excitation at 390 nm, with samples prepared by photoreduction in the presence of EDTA at pH 10.1 (a) and 2-ME (b) at pH 10.1, or through chemical reduction with $Na_2S_2O_4$ at pH 7.4 (c) and pH 13.0 (d).

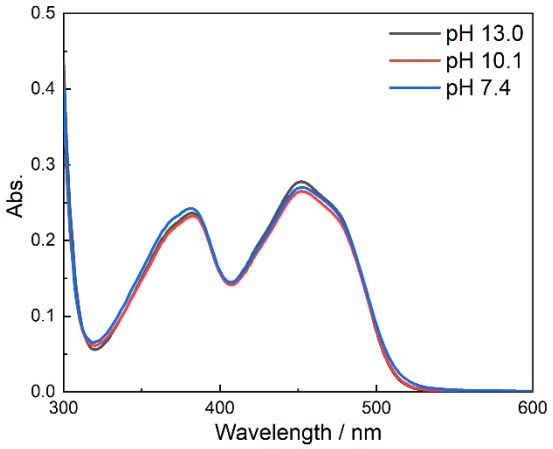

Fig. S20. Steady-state absorption spectra of the freshly prepared FAD_{ox} samples of GOX at different pH values.

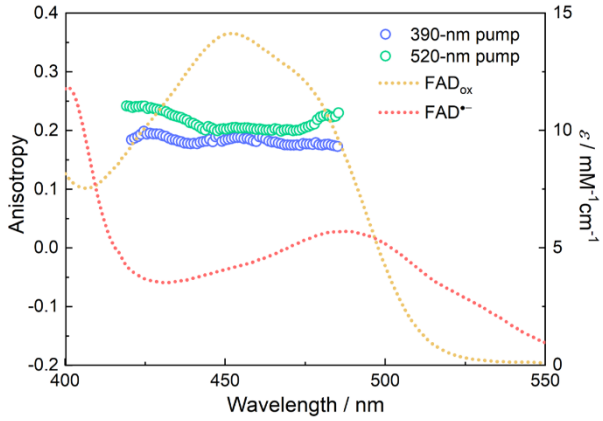

Fig. S21. Transient anisotropy in the induced absorption regions calculated based on polarized DAS of the ~20 ps phase under two excitation conditions in GOX (colored circles). The steady-state absorption spectra of FAD_{ox} and $FAD^{\bullet-}$ in GOX are also shown as references (dashed lines).

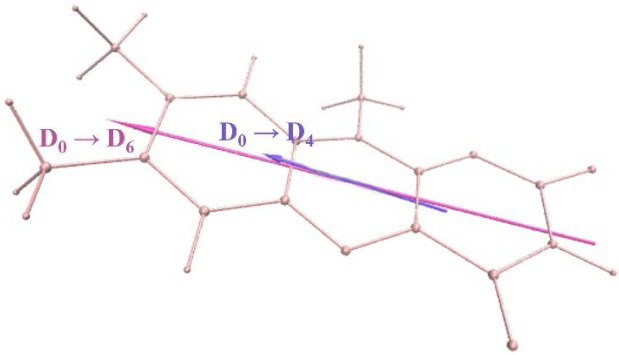

Fig. S22. Orientations of the transition dipole moments of the $D_0 \rightarrow D_4$ and $D_0 \rightarrow D_6$ transitions of an anionic flavin radical from TDDFT calculations.

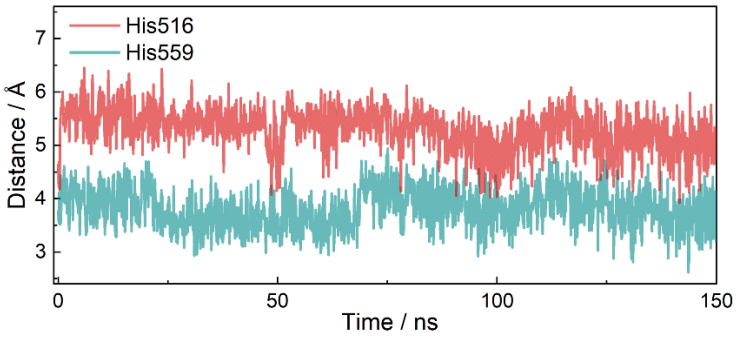

Fig. S23. The minimal ring-to-ring distance between $FAD^{\bullet-}$ and His516 or His559 in the MD simulation of GOX.

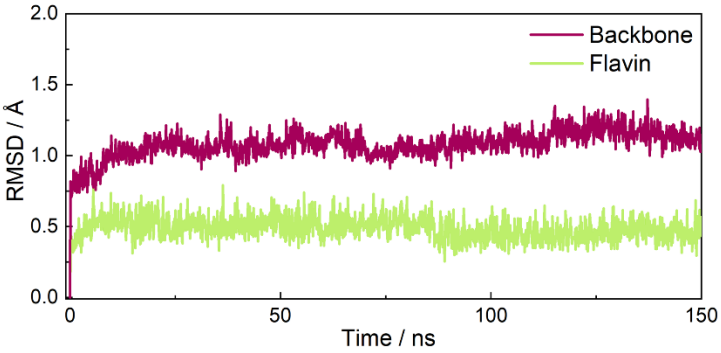

Fig. S24. RMSD for the backbone atoms of the protein and non-hydrogen atoms of $FAD^{\bullet-}$ in GOX in the 150 ns MD simulation.

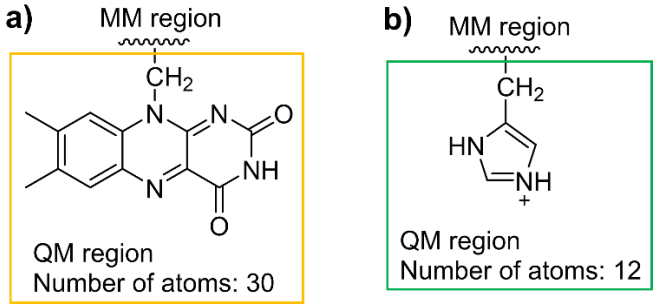

Fig. S25. QM regions employed in the QM/MM calculations of FAD (a) and His559 (b) in GOX.

Supplementary Tables

Table S1. Experimental conditions for preparing reduced flavin species in this study.

Species	Protein	Reductant (chemical reduction)	Hole scavenger (photoreduction)	pH
$FAD^{\bullet-}$	GOX	$Na_2S_2O_4$	-	7.6, 10.1, 13.0
$FAD^{\bullet-}$	GOX	-	EDTA	10.1
$FAD^{\bullet-}$	GOX	-	2-ME	10.1
$FADH^-$	GOX	D(+)-glucose	-	7.6
$FAD^{\bullet-}$	COX	$Na_2S_2O_4$	-	8.1
$FAD^{\bullet-}$	MSOX	$Na_2S_2O_4$	-	8.0, 8.5
$FAD^{\bullet-}$	DAAO	-	2-ME	8.1
$FMN^{\bullet-}$	NMO	P3N	-	8.0

Table S2. Parameters from the global multi-exponential fit for fluorescence decays of flavin species in GOX and COX. The pre-exponential factor of each component is given in parentheses following the time constants.

	τ_1 (ps)	τ_2 (ps)	τ_3 (ps)
FAD_{ox} (GOX)	1.1 (0.62)	4.3 (0.34)	120 (0.04)
$FADH^-$ (GOX)	800 (1.00)		
As-prepared (oxidized) COX	0.29 (0.91)	440 (0.09)	
Reduced COX	0.30 (0.90)	320 (0.10)	

Table S3. Time constants from the global fit of the transient absorption kinetics of anionic flavin radicals (520-nm excitation), as well as positively charged residues close (within 5 Å) to the flavins, in the five flavoprotein oxidases.

Protein	τ (ps)	Close-by positively charged residue
GOX	19	His559, His516
COX	10	His466, Arg89*
MSOX	15	Lys384, Arg49
DAAO	18	Arg283
NMO	21	His133

*For His99, see the main text.

Table S4. Molecular orbital energies of selected residue side chains in the one-electron reduced form. Energies were obtained on the geometry optimized at the ωB97X-D3/ma-def2-TZVP level in vacuum.

Residue	ϵ_{HOMO} (eV)
Arginine	−5.92
Asparagine	−0.14
Histidine (doubly protonated)	−5.24
Histidine (N_ε protonated)	−0.77
Histidine (N_δ protonated)	−0.42
Lysine	−3.77
Methionine	−0.28
Phenylalanine	−0.17
Tyrosine	−0.28
Tryptophan	−0.08
Backbone amide group*	−0.60

**N*-methylacetamide was used as an analog.

Table S5. pK_a calculations based on MDFE simulations. Variables are defined in *Note 6*. Statistical uncertainty in parentheses estimated as twice the standard deviation of block averages, with each data set being divided into five blocks. N/A, not applicable. N/D, not determined.

	With $FAD^{\bullet-}$ (His516, GOX)	With $FADH^-$ (His516, GOX)	Explicit solvent (dipeptide)
ΔG (kcal/mol)	9.9 (0.9)	4.6 (0.5)	1.1 (0.2)
$\Delta\Delta G_{calc}$ (kcal/mol)	8.8 (0.9)	3.5 (0.5)	N/A
pK_a (calc.)	13.5 (0.7)	9.6 (0.4)	N/A
p$K_{a,}$ (exper.)	N/D	8.1*	7.0

*The experimental value is from Ref (42).

Table S6. CHELPG atomic charges of histidine in the neutral radical form. The CHARMM force field atom names are used. The calculations were performed at the ωB97X-D3/ma-def2-TZVP level.

Atom	CHELPG atomic charges
CB	-0.0797
HB1	0.0488
HB2	0.0499
CE1	-0.4904
HE1	0.2135
CD2	-0.2764
HD2	0.1751
ND1	-0.1780
HD1	0.2906
NE2	-0.1887
HE2	0.3081
CG	0.1271

Table S7. Energies in eq. s7 calculated for FAD_{ox}, $FAD^{\bullet-}$, $HisH_2^+$ and $HisH_2^\bullet$. Energies were computed at the PWPB95-D4/def2-QZVPP level with thermostatistical corrections at the ωB97X-D3/ma-def2-TZVP level, and given relative to FAD_{ox} and $HisH_2^+$, respectively; The solvation energies were calculated with the SMD solvation model at the M06-2X/6-31G* level. Geometries were optimized at the ωB97X-D3/ma-def2-TZVP level prior to energy calculations.

	G_g (kJ/mol)	ΔG_{solv} (kJ/mol)	ΔG_s (kJ/mol)
FAD_{ox}	0.0	−73.6	−367.3
$FAD^{\bullet-}$	−176.1	−250.7	
$HisH_2^+$	0.0	−242.4	−178.2
$HisH_2^\bullet$	−389.6	−16.9	

SI References

1. A. Hense, E. Herman, S. Oldemeyer, T. Kottke, Proton transfer to flavin stabilizes the signaling state of the blue light receptor plant cryptochrome. *J. Biol. Chem.* **290**, 1743–1751 (2015).
2. L. Nag, P. Sournia, H. Myllykallio, U. Liebl, M. H. Vos, Identification of the TyrOH•+ radical cation in the flavoenzyme TrmFO. *J. Am. Chem. Soc.* **139**, 11500–11505 (2017).
3. V. Massey, G. Palmer, On the existence of spectrally distinct classes of flavoprotein semiquinones. A new method for the quantitative production of flavoprotein semiquinones. *Biochemistry* **5**, 3181–3189 (1966).
4. D. Su, *et al.*, Fluorescence properties of flavin semiquinone radicals in nitronate monooxygenase. *ChemBioChem* **20**, 1646–1652 (2019).
5. S. P. Laptenok, P. Nuernberger, A. Lukacs, M. H. Vos, in *Methods in molecular biology, fluorescence spectroscopy and microscopy: methods and protocols,* (Humana, New York, 2014), vol. 1076, pp. 321–336.
6. B. Zhuang, D. Seo, A. Aleksandrov, M. H. Vos, Characterization of light-induced, short-lived interacting radicals in the active site of flavoprotein ferredoxin-NADP+ oxidoreductase. *J. Am. Chem. Soc.* **143**, 2757–2768 (2021).
7. J. J. Snellenburg, S. P. Laptenok, R. Seger, K. M. Mullen, I. H. M. van Stokkum, Glotaran: a Java-based graphical user interface for the R package TIMP. *J. Stat. Softw.* **49** (2012).
8. Y. S. Lin, G. De Li, S. P. Mao, J. Da Chai, Long-range corrected hybrid density functionals with improved dispersion corrections. *J. Chem. Theory Comput.* **9**, 263–272 (2013).
9. J. Zheng, X. Xu, D. G. Truhlar, Minimally augmented Karlsruhe basis sets. *Theor. Chem. Acc.* **128**, 295–305 (2011).
10. H. Neugebauer, F. Bohle, M. Bursch, A. Hansen, S. Grimme, Benchmark study of electrochemical redox potentials calculated with semiempirical and DFT methods. *J. Phys. Chem. A* **124**, 7166–7176 (2020).
11. A. V. Marenich, C. J. Cramer, D. G. Truhlar, Universal solvation model based on solute electron density and on a continuum model of the solvent defined by the bulk dielectric constant and atomic surface tensions. *J. Phys. Chem. B* **113**, 6378–6396 (2009).
12. R. F. Ribeiro, A. V. Marenich, C. J. Cramer, D. G. Truhlar, Use of solution-phase vibrational frequencies in continuum models for the free energy of solvation. *J. Phys. Chem. B* **115**, 14556–14562 (2011).
13. F. Neese, The ORCA program system. *Wiley Interdiscip. Rev. Comput. Mol. Sci.* **2**, 73–78 (2012).
14. J. C. Phillips, *et al.*, Scalable molecular dynamics with NAMD. *J. Comput. Chem.* **26**, 1781–1802 (2005).
15. J. Huang, *et al.*, CHARMM36m: an improved force field for folded and intrinsically disordered proteins. *Nat. Methods 2016 141* **14**, 71–73 (2016).
16. W. L. Jorgensen, J. Chandrasekhar, J. D. Madura, R. W. Impey, M. L. Klein, Comparison of simple potential functions for simulating liquid water. *J. Chem. Phys.* **79**, 926–935 (1983).
17. A. Aleksandrov, A molecular mechanics model for flavins. *J. Comp. Chem.* **40**, 2834–2842 (2019).
18. M. H. M. Olsson, C. R. SØndergaard, M. Rostkowski, J. H. Jensen, PROPKA3: Consistent treatment of internal and surface residues in empirical p K a predictions. *J. Chem. Theory Comput.* **7**, 525–537 (2011).
19. T. Simonson, J. Carlsson, D. A. Case, Proton binding to proteins: pKa calculations with explicit and implicit solvent models. *J. Am. Chem. Soc.* **126**, 4167–4180 (2004).
20. T. Darden, D. York, L. Pedersen, Particle mesh Ewald: An N·log(N) method for Ewald sums in large systems. *J. Chem. Phys.* **98**, 10089–10092 (1993).
21. H. J. C. Berendsen, J. P. M. Postma, W. F. van Gunsteren, A. DiNola, J. R. Haak, Molecular dynamics with coupling to an external bath. *J. Chem. Phys.* **81**, 3684 (1998).
22. M. J. Field, The pDynamo program for molecular simulations using hybrid quantum chemical and molecular mechanical potentials. *J. Chem. Theory Comput.* **4**, 1151–1161 (2008).
23. C. M. Breneman, K. B. Wiberg, Determining atom-centered monopoles from molecular electrostatic potentials. The need for high sampling density in formamide conformational

analysis. *J. Comput. Chem.* **11**, 361–373 (1990).
24. L. Zanetti-Polzi, M. Aschi, A. Amadei, I. Daidone, Alternative electron-transfer channels ensure ultrafast deactivation of light-induced excited states in riboflavin binding protein. *J. Phys. Chem. Lett.* **8**, 3321–3327 (2017)
25. A. D. Becke, A new mixing of Hartree-Fock and local density-functional theories. *J. Chem. Phys.* **98**, 1372–1377 (1993).
26. M. M. Francl, *et al.*, Self-consistent molecular orbital methods. XXIII. A polarization-type basis set for second-row elements. *J. Chem. Phys.* **77**, 3654 (1998).
27. B. R. Brooks, *et al.*, CHARMM: A program for macromolecular energy, minimization, and dynamics calculations. *J. Comput. Chem.* **4**, 187–217 (1983).
28. S. C. Harvey, Treatment of electrostatic effects in macromolecular modeling. *Proteins Struct. Funct. Bioinforma.* **5**, 78–92 (1989).
29. V. Massey, M. Stankovich, P. Hemmerich, Light-mediated reduction of flavoproteins with flavins as catalysts. *Biochemistry* **17**, 1–8 (1978).
30. R. Traber, H. E. A. Kramer, P. Hemmerich, Mechanism of light-induced reduction of biological redox centers by amino acids. a flash photolysis study of flavin photoreduction by ethylenediaminetetraacetate and nitrilotriacetate. *Biochemistry*. **21**, 1687–1693 (1982).
31. N. Nunthaboot, *et al.*, Simultaneous analysis of ultrafast fluorescence decays of FMN binding protein and its mutated proteins by molecular dynamic simulation and electron transfer theory. *J. Phys. Chem. B* **112**, 13121–13127 (2008).
32. L. Nag, A. Lukacs, M. H. Vos, Short-lived radical intermediates in the photochemistry of glucose oxidase. *ChemPhysChem* **20**, 1793–1798 (2019).
33. D. Su, C. Smitherman, G. Gadda, A metastable photoinduced protein–flavin adduct in choline oxidase, an enzyme not involved in light-dependent processes. *J. Phys. Chem. B* **124**, 3936–3943 (2020).
34. M. Enescu, L. Lindqvist, B. Soep, Excited-state dynamics of fully reduced flavins and flavoenzymes studied at subpicosecond time resolution. *Photochem. Photobiol.* **68**, 150–156 (1998).
35. F. Lacombat, P. Plaza, M. A. Plamont, A. Espagne, Photoinduced chromophore hydration in the fluorescent protein Dreiklang is triggered by ultrafast excited-state proton transfer coupled to a low-frequency vibration. *J. Phys. Chem. Lett.* **8**, 1489–1495 (2017).
36. P. Müller, K. Brettel, [Ru(bpy)3]2+ as a reference in transient absorption spectroscopy: Differential absorption coefficients for formation of the long-lived 3MLCT excited state. *Photochem. Photobiol. Sci.* **11**, 632–636 (2012).
37. W. W. Parson, *Modern optical spectroscopy: with exercises and examples from biophysics and biochemistry,* (Springer, Berlin, ed. 2, 2015).
38. A. Warshel, F. Sussman, G. King, Free energy of charges in solvated proteins: microscopic calculations using a reversible charging process. *Biochemistry* **25**, 8368–8372 (2002).
39. T. Simonson, Free energy calculations: Approximate methods for biological macromolecules. *Springer Ser. Chem. Phys.* **86**, 423–461 (2007).
40. A. Aleksandrov, T. Simonson, Molecular dynamics simulations of the 30S ribosomal subunit reveal a preferred tetracycline binding site. *J. Am. Chem. Soc.* **130**, 1114–1115 (2008).
41. A. Aleksandrov, J. Proft, W. Hinrichs, T. Simonson, Protonation patterns in tetracycline:Tet repressor recognition: simulations and experiments. *ChemBioChem* **8**, 675–685 (2007).
42. J. P. Roth, J. P. Klinman, Catalysis of electron transfer during activation of O2 by the flavoprotein glucose oxidase. *Proc. Natl. Acad. Sci. U. S. A*. **100**, 62–67 (2003).
43. M. Namazian, M. L. Coote, Accurate calculation of absolute one-electron redox potentials of some para-quinone derivatives in acetonitrile. *J. Phys. Chem. A*. **111**, 7227–7232 (2007).
44. H. Ishikita, E. W. Knapp, Redox potential of quinones in both electron transfer branches of photosystem I. *J. Biol. Chem.* **278**, 52002–52011 (2003).
45. Y.-T. Kao, *et al.*, Ultrafast dynamics and anionic active states of the flavin cofactor in cryptochrome and photolyase. *J. Am. Chem. Soc*. **130**, 7695–7701 (2008).